Shock-induced persistent contact and synchronous re-levitation control in an AMB-rotor system

Abstract:

Active magnetic bearings (AMBs) have limited dynamic load capacity due to magnetic material field saturation. Hence, large external disturbances (such as shock loads) may cause contact between the rotor and touchdown bearings (TDBs), which may evolve into complex dynamic behaviour and damage the machine. This paper considers the shock responses of a rotor and viable re-levitation control options when the AMB is still functional. Bi-stable responses and persistent forward rubbing are observed in an experimental flexible AMB-rotor facility and its numerical model. The standard control action for a contact-free rotor state would not be appropriate due to phase changes and displacement amplitude differences in the frequency response. To destabilise the limit cycle responses and restore contact-free levitation, open-loop phase search based synchronous compensation (PSSC) control and synchronous motion compensation (SMC) control are designed, which are activated when contact is detected. Stability of the control system and the effectiveness of these two re-levitation control methods are verified by simulation and experimental results. It is also found by comparison that the efficiency of PSSC depends on the phase difference (incorrect phases may degrade rotor response), while the SMC consumes more computing effort.

1. Introduction

Interactions between a rotor and touchdown bearing (TDB), caused by large external disturbances or overloads, may result in problematic dynamic behaviour of the rotor. Prolonged exposure to these severe dynamics will cause TDB degradation, requiring regular replacements. This will lead to outage periods that are costly in terms of missed productivity [1]. Therefore, a clear aim is to restore contact-free levitation through available control capability in an efficient manner. This would be beneficial for maintaining the normal operation of the maglev rotor under shock loads and for extending the life of the TDB [2].

Accordingly, a fuller understanding of rotor dynamic behaviour in rotor/TDB contact conditions is necessary. Most related studies have dealt with the rotor dynamics following a drop condition. This is essentially a purely passive dynamic process, as it is considered that all control capability associated with an AMB no longer exists [3]. Modelling, simulations, and tests on an industrial scale have been undertaken [4]–[7], and detailed predictions have become possible.

However, the coupling of functional AMBs makes the dynamic behaviour of a rotor more complex. Keogh and Cole [2] analysed the variable contact mode and stability of AMB-rotor systems. Simulation and experiment results indicated that changes in synchronous vibration amplitude and phase induced by contact events cause existing

controllers to be ineffective in attenuating rotor displacements [8]. Some of the issues that should be considered when assessing rotor dynamic coupling with contact events and the options for using an active TDB to aid control have been outlined [9]. Under certain conditions, rotor dynamic conditions may develop to the point where initial rotor bouncing continues and transgresses into persistent rubbing (or combined bounce and rub), or even to the point of becoming chaotic unless further control action is taken or other inputs are applied [1].

It is desirable to destabilise such persistent contact because it will cause an accumulation of damage and limit TDB life. Further, as inherent unbalance may be the main factor for persistent contact, some synchronous unbalance force compensation-based controllers have been studied [3], [10]. Phase changes caused by contact also need to be considered, and some robust control related algorithms have been proposed [11]–[13]. Ulbrich *et al*. [14] considered electromechanical actuation of a TDB, while Cade *et al*. [15] and Li *et al*. [16] implemented piezoelectric actuation of a TDB. The option of an active TDB offers additional control capabilities with the potential of restoring contact-free rotor levitation. However, an active TDB involves a more complex structure and would incur higher costs.

To date, there is a lack of published work relating to shock response and corresponding automatic re-levitation control of AMB-rotor systems. Jarroux *et al*. [17], [18] observed the dynamic behaviour of an AMB-rotor system with strong base motion. The 6000 rpm rotor, which was placed on a shock platform and experienced sinusoidal disturbance (0.1–1.1 G amplitude at 20 Hz), returned to a stable state after rubbing with the TDBs for a short time. Hawkins *et al*. [19] presented the floating shock platform test results for an AMB supported chiller compressor for MIL-S-901D shock certification. After experiencing limited contact between the rotor and TDBs, the rotor returned to a stable operating state. Recently, nonlinear dynamic behaviour and parameter analysis of an AMB-rotor system subjected to strong base shock excitation have been studied by simulation [20].

The aim of this paper is to provide an understanding of the bi-stable phenomenon and possible contact faults caused by shock loads. This is achieved through analytical expressions, nonlinear dynamic simulations, and experimental results from an AMB-flexible rotor facility. Then, open-loop phase search based synchronous compensation (PSSC) control and synchronous unbalance force rejection (SMC) control are designed and applied, respectively, to destabilise the limit cycle responses. Comparisons between these two control actions are also discussed with relevance to implementation. The new aspect of this paper is that it provides insights into shock contact in the bi-stable area and enables real-time detection and online control actions to stabilise contact-free operation of the rotor, even in the event of shock loads.

2. Bi-stable phenomenon

2.1 Conditions for bi-stable phenomenon

A synchronously rotating reference frame (u, v) is used to analyse the existence of persistent contact clearly. In Fig. 1, the left view (a) is a contact-free case that the

unbalance and synchronous AMB forces under a proportional-integral-derivative (PID) control drive the rotor to point E. This point lies within the clearance circle. The phase angle between the force and response ϕ is determined by the AMB characteristics, unbalance mass, and rotational speed. The right view (b) shows a rotor in forward synchronous rubbing. The rotor is driven to point C on the clearance circle under the effect of the unbalance force f_u, the normal contact force f_c, the tangential friction force μf_c, and the resultant synchronous AMB force f_s. If these forces are balanced, persistent contact may occur, which means that bi-stable responses (one without contact and one involving contact) exist.

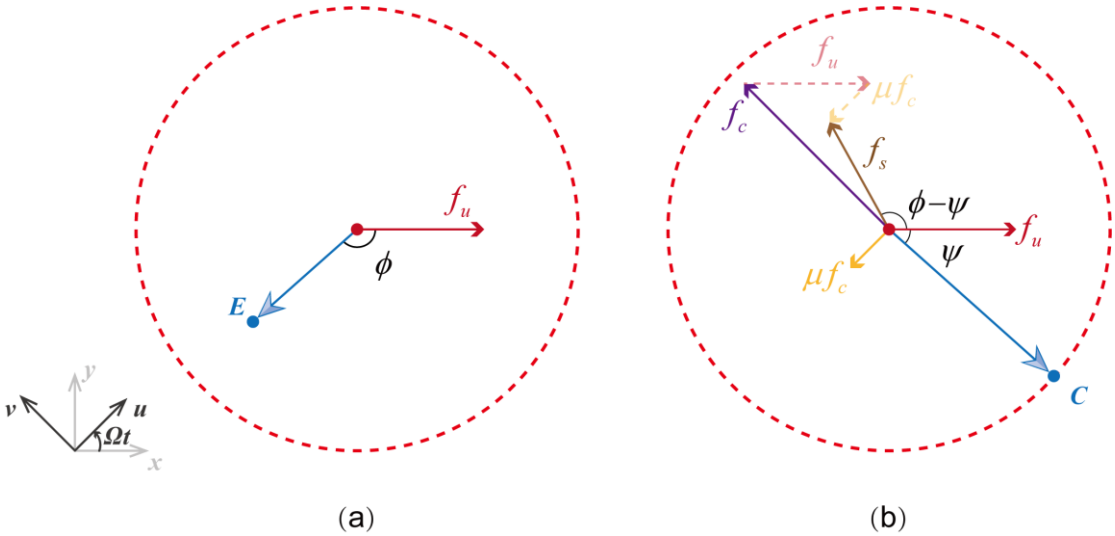

Figure 1 Synchronous orbits viewed in a synchronously rotating reference frame. (a) contact-free orbit *E* induced by the unbalance force f_u; (b) persistent contact orbit *C* induced by unbalance force f_u, normal contact force f_c, tangential friction force μf_c, and resultant AMB force f_s.

For a symmetric AMB-rotor system, previous studies have proved that the bi-stable responses may exist when angle ψ satisfies Eq. (1) [21]:

$$\begin{cases} \dfrac{f_c}{f_u} = \dfrac{1}{(1+i\mu)}\left(e^{i\psi} - \dfrac{c}{r_E}e^{i\phi}\right) \\ \mathrm{Im}\left(\dfrac{f_c}{f_u}\right) = 0 \\ \mathrm{Re}\left(\dfrac{f_c}{f_u}\right) > 0 \end{cases} \tag{1}$$

where μ is the friction coefficient, c is the maximum gap between the rotor and the

TDB, and r_E is the steady motion radius of the non-contacting orbit.

However, it may be difficult to deduce a general theoretical solution of bi-stable conditions for a general multi-disk AMB-rotor system by assuming a persistent contact motion. Hence, research on the bi-stable condition of asymmetric AMB-rotor systems requires numerical simulations and impact-rub experiments.

2.2 Experimental study

The experimental AMB-flexible rotor facility is shown in Fig. 2. The rotor is mounted horizontally on two radial AMBs. Eight current-controlled pulse width modulated amplifiers power the magnet coils with a bias current of 4.3 A, giving an open-loop bearing negative stiffness of 2×10^6 N/m, a current gain of 487 N/A, and a peak filter control force of approximately 1,500 N.

The rotor shaft is 2 m long with four 10 kg disks of radii 10 cm mounted on it to provide added inertia, giving a total mass of 100 kg. The first forward and backward flexural mode critical speeds are 25.3 Hz and 26.5 Hz, respectively. The rotor is driven through a flexible coupling by a motor whose maximum rotational speed is 6,000 rpm.

Four TDBs (A, B, C, D) are configured. Rolling element bearings (B, C) with a nominal radial clearance (0.7 mm) prevent contact between the AMB laminations and rotor, which have a radial clearance of 1.2 mm. Additionally, bronze bushes (A, D) with nominal radial clearances 0.4 and 0.8 mm are located close to the rotor disks to prevent further rotor excursions.

Lateral displacements of the rotor are measured using eight eddy current displacement sensors in four axial planes, as shown in Fig. 2. Each sensor pair is arranged at $\pm45°$ either side of vertical.

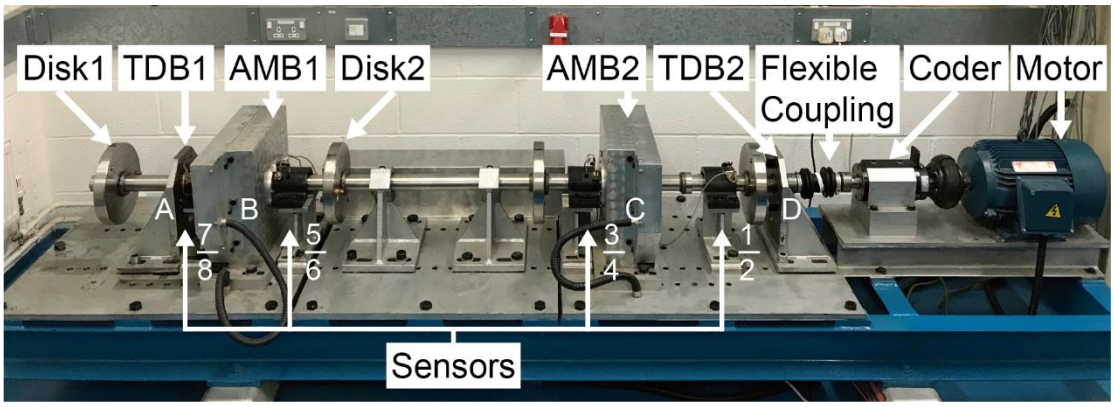

Figure 2 AMB-flexible rotor facility

Local PID displacement feedback control of the bearings provided stable rotor levitation and modal damping. The motor was controlled by a frequency converter. A 100 g • cm unbalance was added to Disk2.

To obtain dynamic conditions of the bi-stable without/with contact phenomenon of the AMB-rotor facility by experiments, the rotating frequency was slowly increased from 0 to 40 Hz and then reduced at a similar rate. Figure 3 shows the synchronous frequency response measurements undertaken in the plane of the sensor pair associated with TDB1.

Figure 3 indicates that the rotor radial displacement at TDB1 increases with frequency up to 20 Hz (due to system resonance) until reaching TDB1 radial clearance. Below this rotational speed, the rotor was not in contact with the TDB1. Increasing the rotating frequency above 20 Hz through to 34 Hz drives the rotor into TDB1 contact, with rotor radial displacements of approximately 0.4 mm. Beyond 34 Hz through to 40 Hz, contact is lost and the rotor radial displacement drops to a post-resonance level. The forcing frequency was then decreased and contact was experienced only from 26 Hz to 22 Hz. This hysteresis effect in the system response arises from the nonlinear characteristics of the rotor/AMB/TDB system. This clearly shows evidence of bi-stable responses from 26 to 34 Hz, with and without rotor/TDB contact.

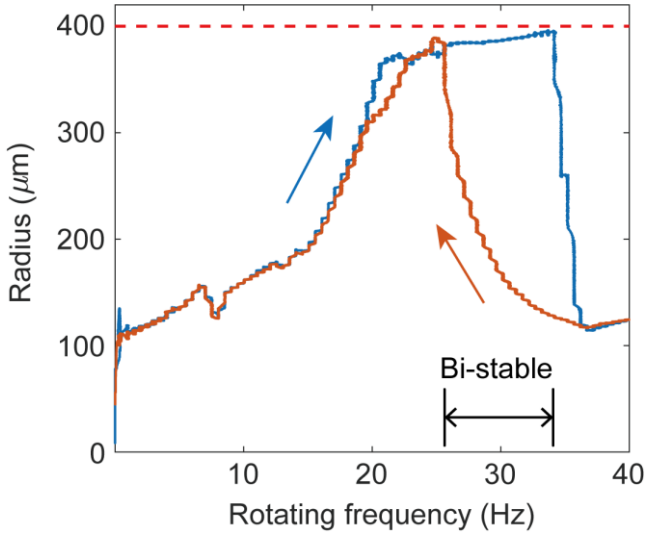

Figure 3. Radial displacements of rotor, at TDB1 with gradual increase and decrease of the rotating force frequency, 100 g • cm unbalance on Disk2.

2.3 Potential trigger condition – shock loads

Although steady persistent contact may exist, the conditions of its occurrence (from point *E* to *C* in Fig. 1) remain unclear. The amplitude of the rotor's synchronous frequency response is generally designed to be within the gap between the rotor and TDB; hence, rotor-TDB contact conditions do not exist. However, shock loads that rotating machines (especially onboard machines) may encounter during normal operation can lead to contact between the rotor and the TDBs, resulting in complex nonlinear vibrations and machine damage [17], [20], [22]. Therefore, it is necessary to investigate shock-induced contact response.

For the AMB-flexible rotor bearing facility with the amplitude-frequency characteristics presented previously, an instantaneous shock force was applied to the rotor by applying current impulses to both AMBs. This was conducted when the rotor was running at different rotating speeds in contact-free conditions. The current impulse was in the form of a half-sine signal with a period of 1.2 ms. Experimental results indicated that shock loads can cause persistent rotor contact in the bi-stable area (from an orange point to a blue point in the bi-stable area in Fig. 3). Moreover, the larger the whirl radius before the shock, the easier it is to jump to a stable contact mode response.

Figures 4(a) and (b), respectively, present the rotor trajectory and corresponding radius at TDB1 of shock responses with an initial rotating frequency of 28 Hz. Under

the effect of inherent unbalance, the rotor whirled in the forward sense with a very small motion radius of 0.2 mm before the shock was applied. After the shock input, the rotor bounced sharply, which then evolved into a persistent contact (forward rubbing) under the combined action of the unbalanced force, nonlinear electromagnetic force, normal restoring force, and tangential dry friction. The motion radius fluctuated around the maximum gap value, and the frequency spectrum analysis indicated that the forward rubbing motion and rotational speed were at the same frequency.

Figures 4(c) and (d), respectively, present the rotor trajectory and corresponding radius at TDB1 for shock responses with an initial rotating frequency of 35 Hz. Like the previous section, under the effect of inherent unbalance, the rotor whirled forward with a very small motion radius of motion of 0.1 mm before the shock, and the rotor vibrated sharply when the shock was applied. However, the shock contact time was short and the rotor then gradually recovered to become contact-free at the centre with the original whirl radius.

Therefore, a shock load is one of the potential trigger conditions that may cause persistent contact. As contact continues, the TDB and rotor will be severely worn or even deformed due to persistent contact, dry friction, and thermal effects. Figure 5 shows he damage to the rotor and TDB caused by contact experiments with a total contact time of no more than 1 min. The experimental results demonstrate the potential hazards caused by shock disturbances to the rotor under bi-stable operating conditions.

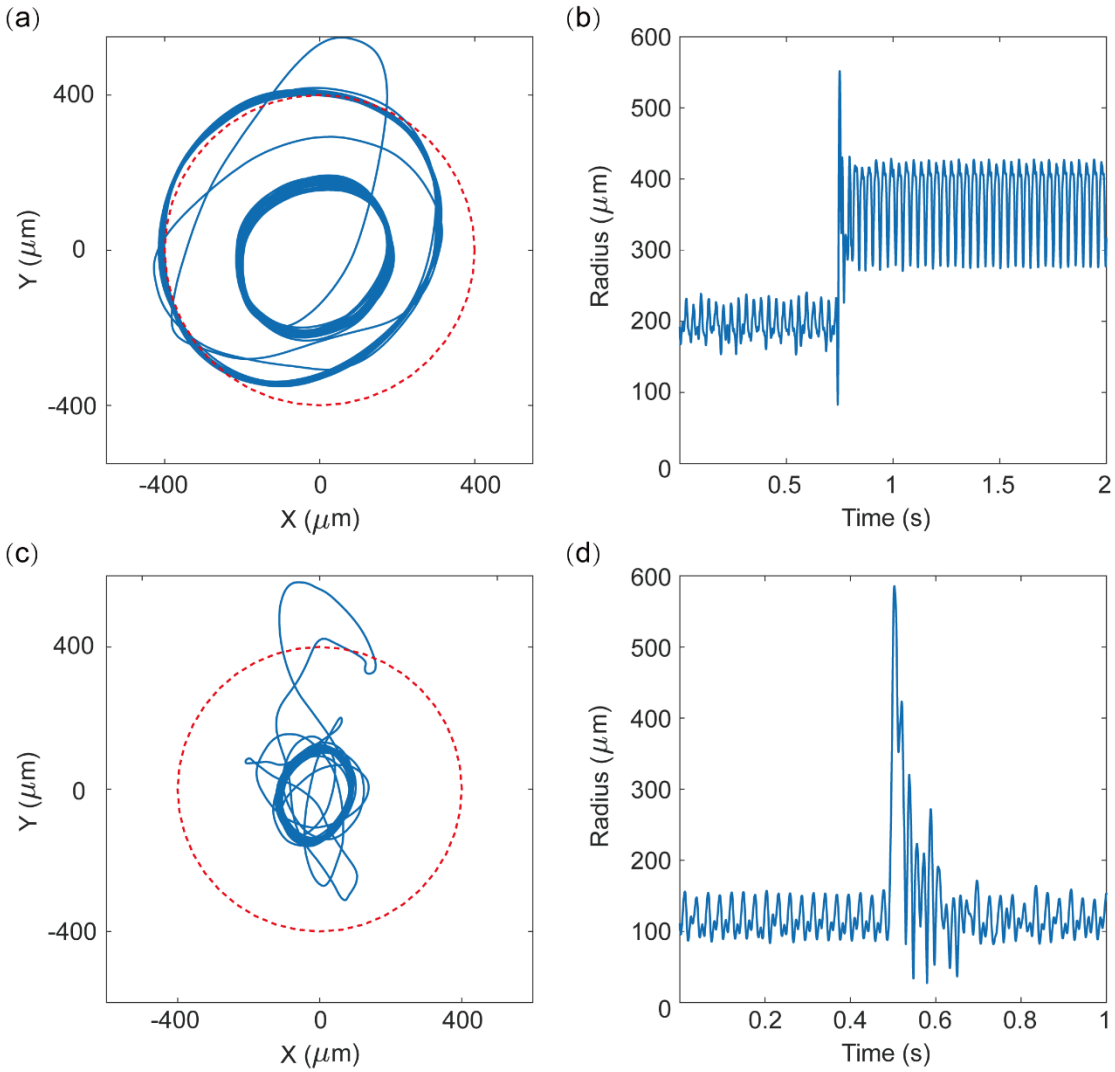

Figure 4. Experimental results of shock responses. (a) and (c) are rotor trajectories at TDB1 with initial running frequencies of 28 and 35 Hz, respectively; (b) and (d) show the corresponding motion radii.

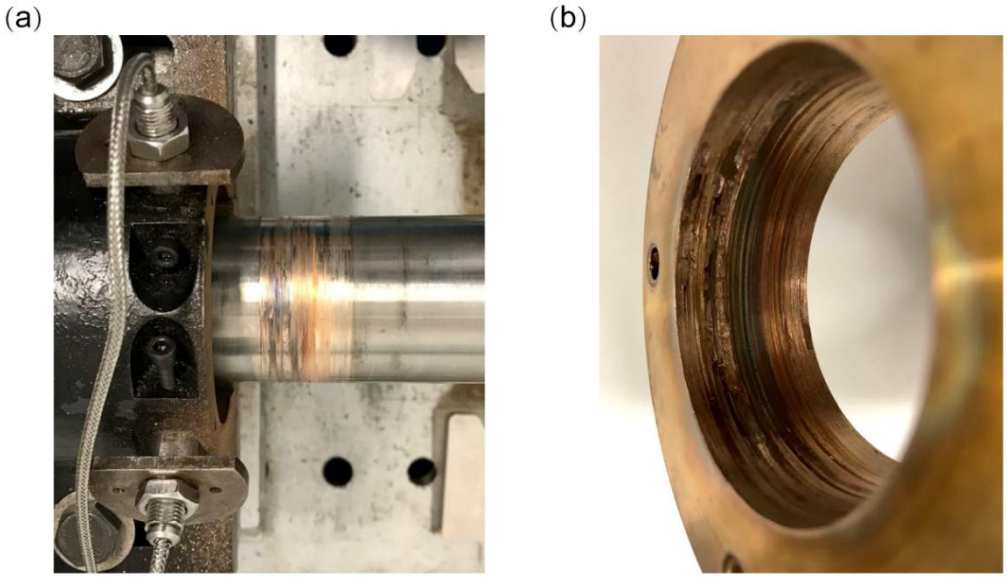

Figure 5. Damage to the rotor and TDB caused by continuous contact at 30 Hz.

3. Dynamic modelling and simulation

3.1 Rotor/AMB/TDB system

As shock contact experiments are destructive, a numerical model was generated to investigate the shock contact and re-levitation control problem. The shaft was divided into 16 beam elements using the finite element methodology of Nelson and McVaugh [23], as shown in Fig. 6. The unbalance forces, AMB forces, contact forces and shock loads were applied to the corresponding nodes.

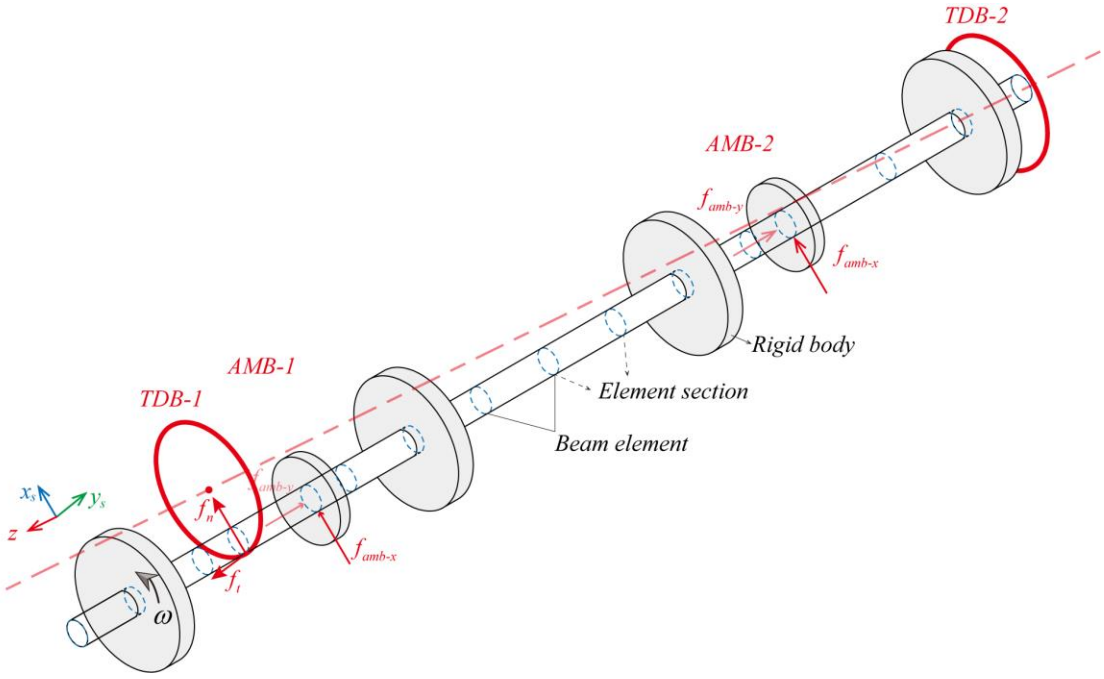

Figure 6. Finite element model of the AMB-flexible rotor facility considering rotor/TDB contact.

The AMB force components in the x- and y-axes applied to the rotor at corresponding nodes are written as follows:

$$f_{amb} = \frac{k_f}{k_s} \tanh k_s \left(\frac{(I_0 + I_c)^2}{(c - z)^2} - \frac{(I_0 - I_c)^2}{(c + z)^2} \right) \tag{2}$$

where $z = x_r$ or y_r denotes the rotor displacement from the AMB magnetic centre, and c is the effective magnetic gap. The bias and control currents (I_0 and I_c) are direction dependent. The AMB stator and rotor iron will have a magnetic flux saturation limit, which is represented empirically by the tanh function, resulting in a maximum AMB radial force of k_f / k_s, where $k_f = \mu_0 N^2 A$ and k_s is a saturation constant.

Since the AMB system is inherently unstable, a PID controller was applied to

realise stable rotor levitation by calculating the control current based on the error between the reference value and the signal from the displacement transducer.

The rotor/TDB contact model in the contact plane is drawn in Fig 7 (a). O_b and O_r are geometric centre of the TDB and the rotor, respectively. The TDB is of the bushing type and is supported by high stiffness springs and dampers. The contact state between the rotor and the TDB depends on the penetration δ. When $\delta > 0$, the rotor will be subjected to a normal restoring contact force f_n and tangential contact force f_t. The nonlinear normal restoring contact force/deflection relation is contained by an empirical model, as shown in Fig 7 (b).

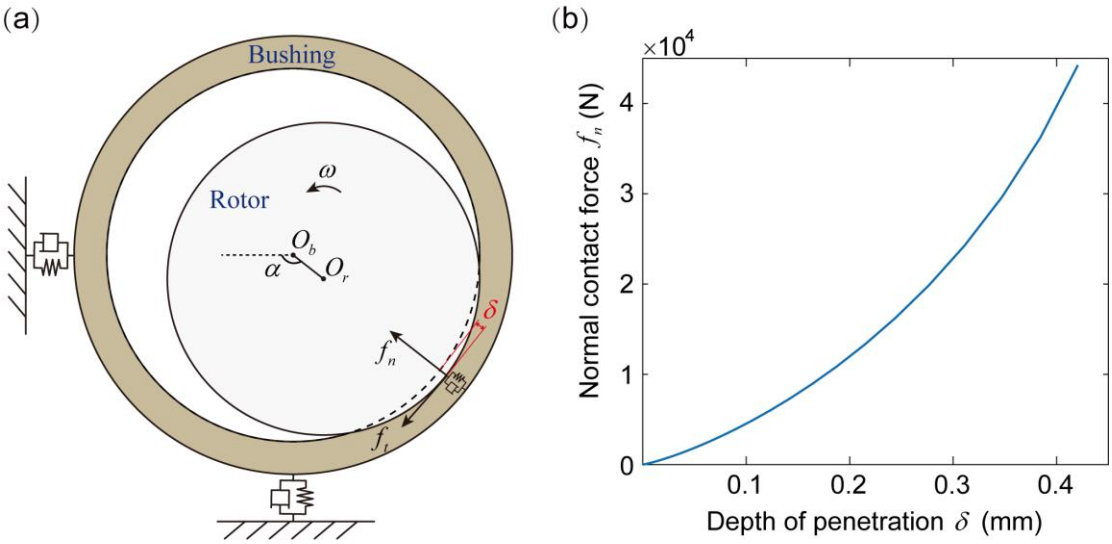

Figure 7. (a) Rotor/TDB contact model; (b) Empirical model of the nonlinear contact force/deflection relation.

A smooth Coulomb friction model, which is a variation of the classic Coulomb model, is adopted here to avoid any numerical difficulties. The friction force f_t is calculated by

$$f_t = STEP\left(v_r, v_s, -\mu, v_s, \mu\right) \tag{3}$$

where μ is the friction coefficient, and v_r is the critical velocity for distinguishing between sliding and rolling. The term v_r is the relative speed at the contact point between the rotor and TDB, which can be calculated as

$$v_r = \omega \cdot r + v_t \tag{4}$$

where $v_t = (\dot{y}_r - \dot{y}_b)\cos\alpha - (\dot{x}_r - \dot{x}_b)\sin\alpha$, $\alpha = \arctan\left(\frac{y_r - y_b}{x_r - x_b}\right)$.

The contact force vector f_c containing the normal restoring force and tangential friction, is given by

$$f_c = \begin{bmatrix} -\cos\alpha & \sin\alpha \\ -\sin\alpha & -\cos\alpha \end{bmatrix} \begin{bmatrix} f_n \\ f_t \end{bmatrix} \tag{5}$$

Finally, the governing equation of the system can be written in a matrix-vector form as follows:

$$\mathbf{M}\ddot{\mathbf{q}} + (\mathbf{C} + \dot{\varphi}\mathbf{G})\dot{\mathbf{q}} + (\mathbf{K} + \dot{\varphi}\mathbf{K}_{ST})\mathbf{q} = \mathbf{f}_u + \mathbf{f}_{amb} + \mathbf{f}_c \tag{6}$$

$$\mathbf{f}_u = \dot{\varphi}^2 \begin{bmatrix} 0 \\ \vdots \\ me\cos\varphi \\ me\sin\varphi \\ \vdots \\ 0 \end{bmatrix} + \ddot{\varphi} \begin{bmatrix} 0 \\ \vdots \\ \sin\varphi \\ \cos\varphi \\ \vdots \\ 0 \end{bmatrix}, \mathbf{f}_{amb} = \begin{bmatrix} 0 \\ \vdots \\ f_{amb-x} \\ f_{amb-y} \\ \vdots \\ 0 \end{bmatrix}, \mathbf{f}_c = \begin{bmatrix} 0 \\ \vdots \\ f_c \\ \vdots \\ 0 \end{bmatrix} \tag{7}$$

Here, $\mathbf{q}$ is the generalised coordinate vector of finite element nodes; $\mathbf{M}$, $\mathbf{K}$, $\mathbf{C}$ and $\mathbf{G}$ are mass, stiffness, damping and gyroscopic matrices; $\mathbf{K}_{ST}$ is the stiffness matrix for transient motion; $\mathbf{f}_u$, $\mathbf{f}_{amb}$ and $\mathbf{f}_c$ are the unbalance force, AMB force, and contact force vectors, respectively; and φ is the rotational angle of the rotor.

3.2 Model verification

This section demonstrates the effectiveness of the established numerical model. First, the acceleration and deceleration processes of the AMB/rotor system (with unbalance mass) were carried out. The rotational frequency was increased from 0 to 40 Hz and then reduced at a similar rate. The radial motion radius of the node of TDB1 is shown in Fig. 8. Comparing with the results in Fig. 3, the measured rotor motion radius can be described qualitatively by the numerical model. The rotor responses of the numerical model and experiment facility were almost the same, both for the acceleration and deceleration processes. The whirling radius error in the non-contact state is due to the slight bending of the rotor of the test facility. The contact and non-contact regions are obvious from the Fig. 8. There is a bi-stable region corresponding to Fig. 3 between 26 Hz and 33 Hz.

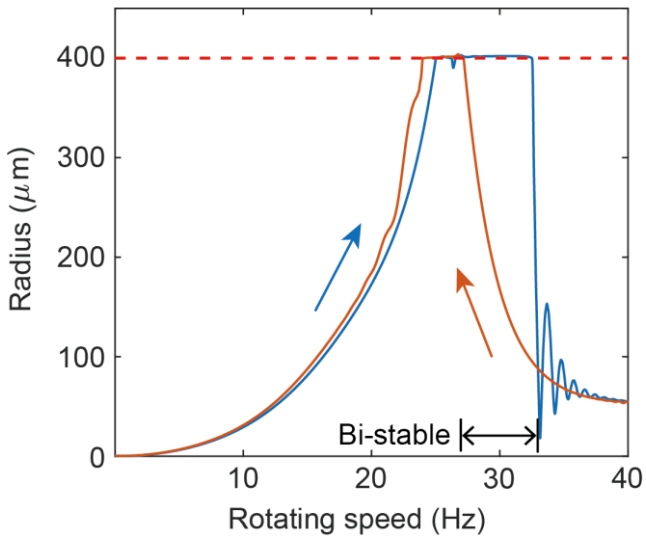

Figure 8. Simulation results of radial motion radius of the rotor at TDB1 with gradual increase and decrease of the rotating force frequency.

To verify the model further, motions of the rotor when subjected to a shock force at a constant rotational frequency were simulated. Figures 9(a) and (b) show the simulation of rotor trajectories at TDB1 with a rotating frequency of 28 Hz (in the bi-stable area) in fixed and synchronously rotating reference frames, respectively. In Fig. 9(a), the rotor experienced transient rebounds that developed into a full forward rub involving persistent contact. In Fig. 9(b), the shock load leads the rotor orbit from the red dot to the green triangle. Figures 9(c) and (d) show the simulation of rotor trajectories at TDB1 with a rotating frequency of 35 Hz in fixed and synchronously rotating reference frames, respectively. In Fig. 9(c), the rotor experienced transient rebounds then resumed a non-contact whirling motion. In Fig. 9(d), the shock load led the rotor orbit from the red dot to the contact status and finally back to the red dot. Compared with the results in Fig. 4(a) and (c), this numerical validation provides confidence considering the prediction of the nonlinear dynamic behaviour of the maglev rotor involving a shock contact. Hence, the established numerical model can be used to study impact-rub dynamics and the ensuing re-levitation control algorithm.

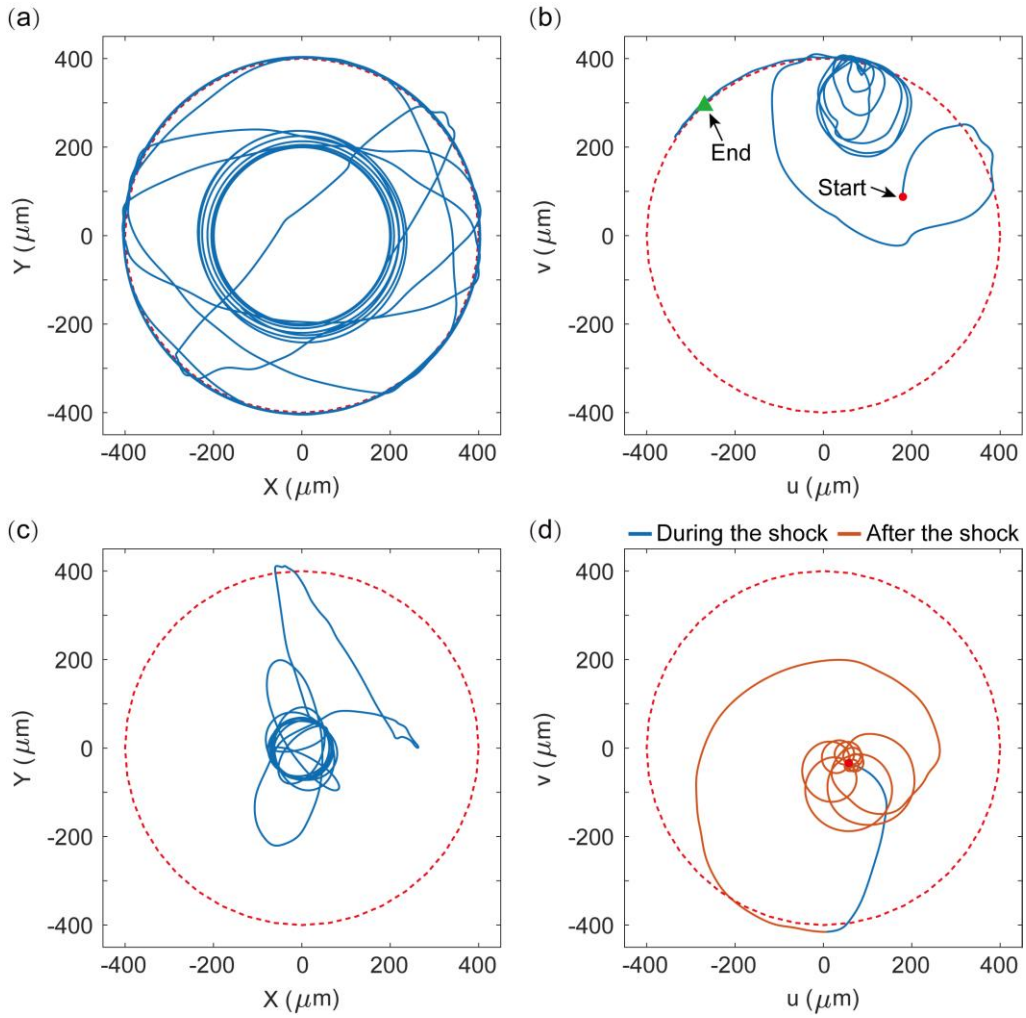

Figure 9. Simulation of rotor trajectories at TDB1 of shock responses with initial rotational frequencies of 28 and 35 Hz. (a) and (c) in a fixed reference frame (*x, y*); (b) and (d) in a synchronously rotating reference frame (*u, v*).

4. Re-levitation control

4.1 PSSC control

The desirable course of action to restore a rotor from steady persistent contact is through application of automatic re-levitation control by AMBs (if still functional). Through the above study, the key to re-levitation control is destabilising the force equilibrium in Fig. 1(b).

A simple idea is to use an extra synchronous compensation AMB force f_d that is generated with open-loop control (as shown in Fig. 10) to destabilise the force equilibrium. In this open-loop synchronous control, determining the amplitude and phase of the force f_d is key for the control algorithm. While the analysis of force equilibrium uses the unbalance force vector as the benchmark, prior knowledge for the amplitude f_u and initial phase angle θ (see Fig. 11 (a)) of unbalance force may not

be available in practical industrial applications. Therefore, the relative phase angle between f_d and the benchmark f_u is hard to obtain, although the initial phase angle α of f_d (in Fig. 11(b)) can be determined by the moment when the re-levitation control is applied.

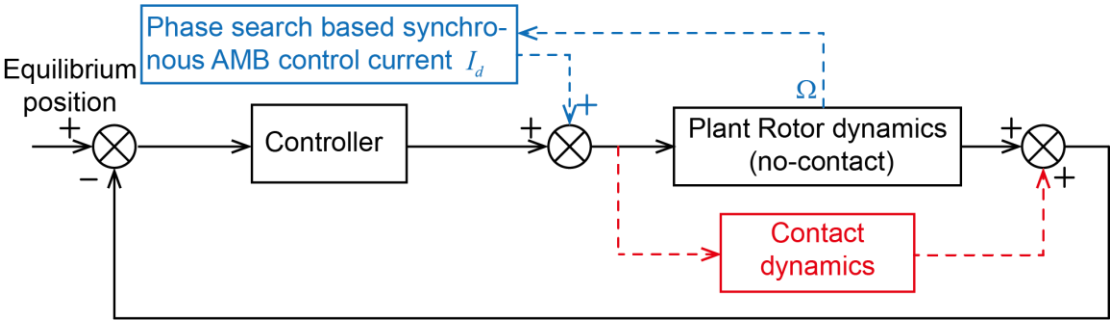

Figure 10. Open-loop phase search based synchronous compensation (PSSC) control diagram

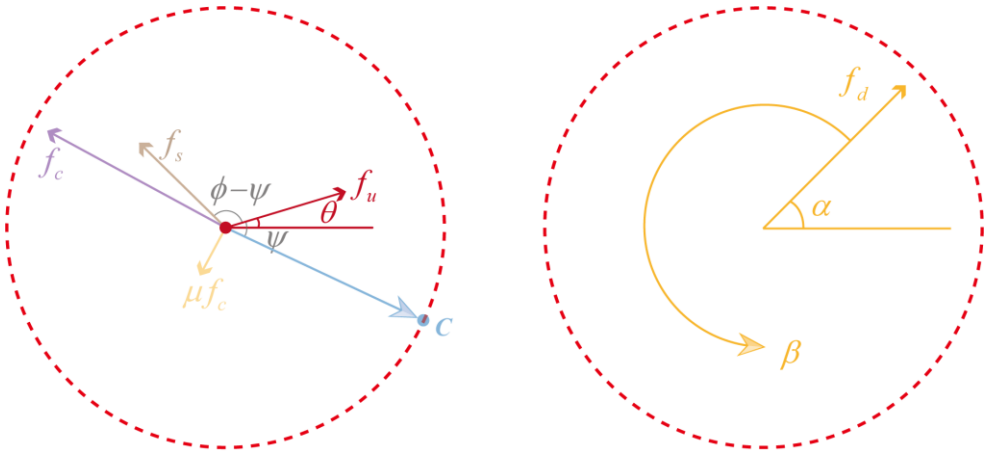

Figure 11. Problem and strategy of open-loop synchronous control. (a) unknown information about unbalance force f_u ; (b) assistant synchronous AMB force vector f_d .

To solve this problem, a phase search based synchronous compensation (PSSC) control is proposed. The control flow chart is presented in Fig. 12.

(1) Initially, the rotor status is monitored in real-time, and displacement sensor data at the TDB are recorded into a short buffer at a certain sampling rate.

(2) The motion radius $r_{TDB}(n)=\sqrt{x_{TDB}(n)^2+y_{TDB}(n)^2}$ is calculated from the short buffer, and the mean value $\bar{r}_{TDB}(n)$ is compared to r_1. Due to the influence of

misalignment, r_1 is generally slightly less than the radial clearance between the rotor and the TDB. If $\overline{r}_{TDB}(n) < r_1$, this means contact does not occur. The control current signals at each pair of coils are recorded into a long buffer to obtain the control currents in normal operation. Conversely, if $\overline{r}_{TDB}(n) > r_1$, a synchronous compensation current is applied, which is calculated as follows:

$$\mathbf{I}_d = \mathbf{I}_1 e^{i(\Omega t+\beta)}$$

(3) Then, the motion radius of the rotor at TDB is calculated and compared with r_2, which needs to be less than the minimum pulsating motion radius of the rotor in continuous contact status. Generally, r_2 can be set as a middle value between r_1 and the whirling radius in non-contact status. If $\sqrt{x_{TDB}{}^2 + y_{TDB}{}^2} < r_2$, the synchronous compensation current $\mathbf{I}_d$ will act for a while (Δt) and then return to zero. Otherwise, β updates with a ramp-like change over time, as shown in Fig. 13.

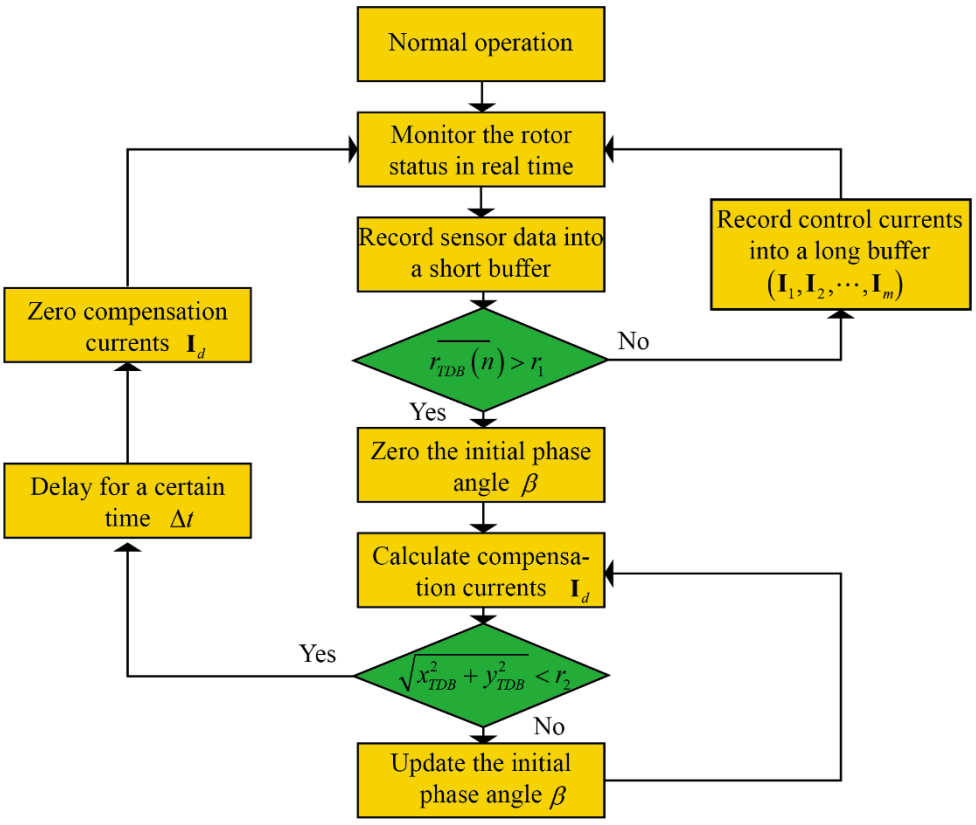

Figure 12. Control flow chart of PSSC

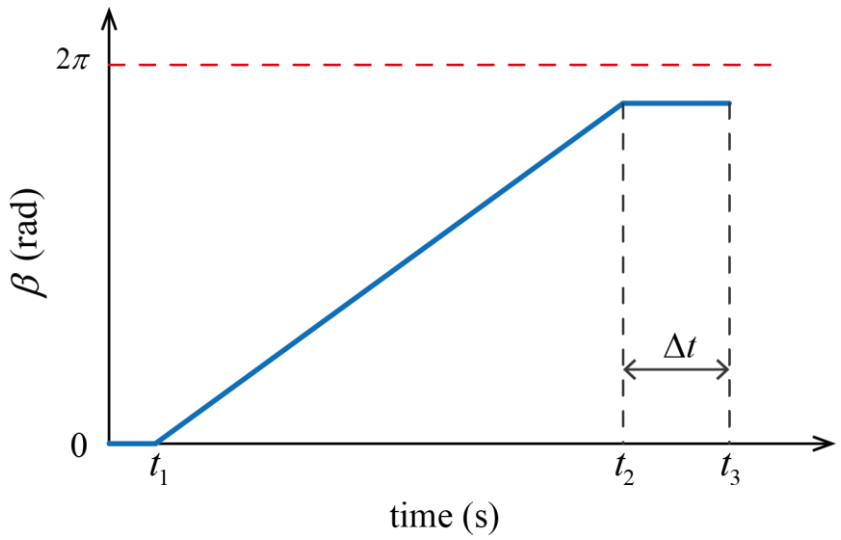

Figure 13. Update method of phase angle β

Figures 14(a) and (b), respectively, show the simulation results of rotor trajectories at TDB1 in a fixed reference frame (*x, y*) and in a synchronously rotating reference frame (*u, v*), when PSSC control is applied for shock contact. Here, r_1 was set to 380 μm and r_2 to 300 μm. The blue line represents the dynamic behaviour of the shock contact process before the action of PSSC control, while the orange line represents the dynamic behaviour after the action of PSSC control. Figure 14(b) indicates that the PSSC control restores the rotor orbit from the green triangle to the red dot. The rotor motion radius and phase angle β of the synchronous AMB force in this process are plotted in Fig. 14(c). The rotational frequency was 30 Hz, and the rotor started persistent forward rubbing after experiencing a shock load. After approximately 0.15 s, the PSSC was activated. However, contact continued, meaning the stability of force equilibrium was not destroyed successfully. Hence, the direction of the synchronous compensation AMB force f_d started to change by searching the phase angle β in a ramp-like way. The radius of rotor motion reduced to below r_2 when β reached 5.09 rad (292°). The synchronous compensation current $\mathbf{I}_d$ acted with this phase angle for 0.1 s and then returned to zero. The rotor recovered under the action of the synchronous compensation current with an appropriate phase.

The experimental results are shown in the Fig. 14(d). There was a slight change on the motion radius of the rotor when the PSSC controller was activated. However, the rotor did not restore immediately. When β reached 5.25 rad (301°) the rotor successfully recovered to non-contact status. The experimental results are consistent

with the simulation results, verifying the effectiveness of the control method. Due to measurement noise, the motion radius is the result of the low-pass filtering. Further, the rotor trajectory at TDB1 is not drawn here.

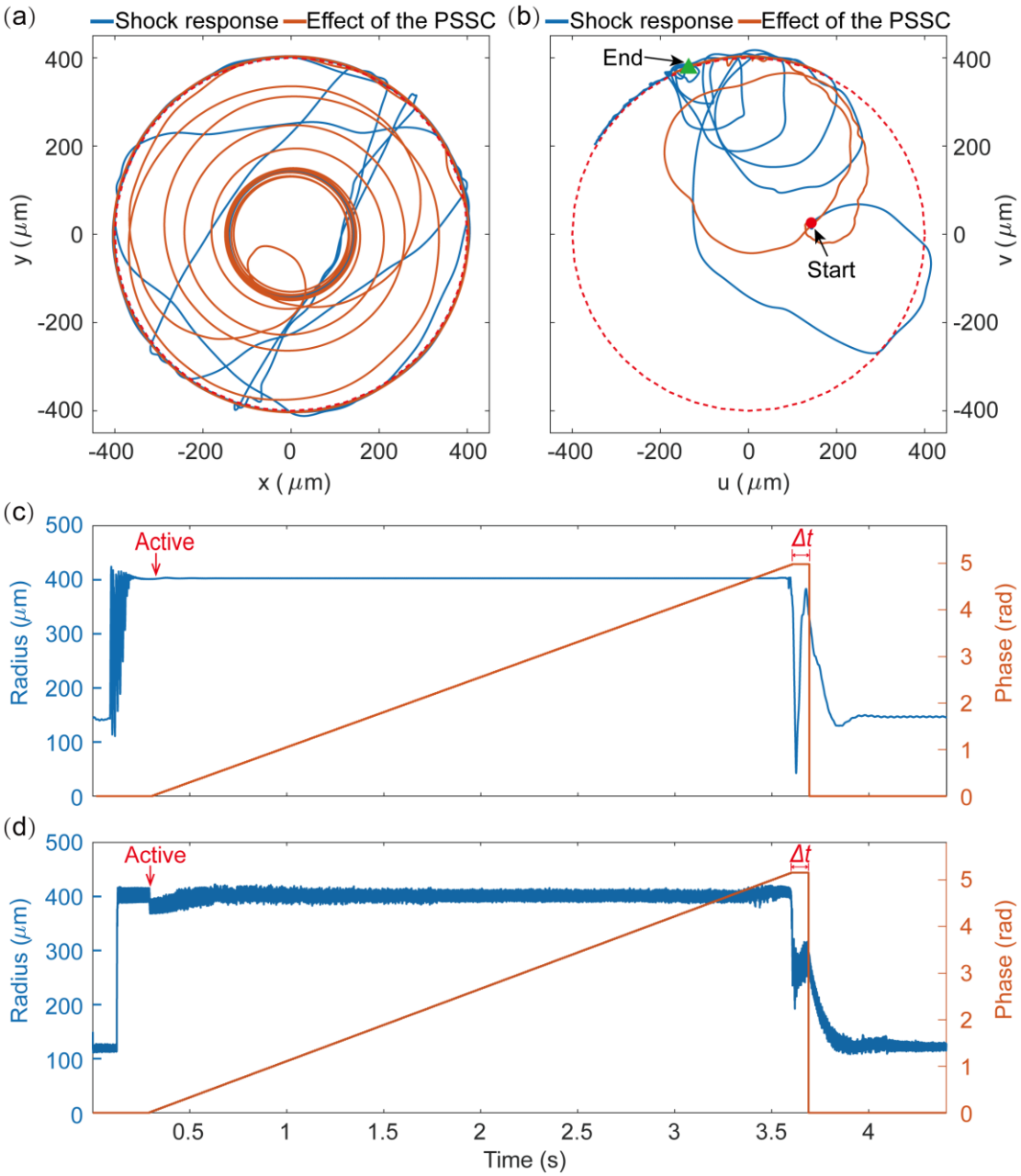

Figure 14. Simulation and experimental results of PSSC control. (a) rotor trajectory at TDB1 in a fixed reference frame (x, y); (b) rotor trajectory at TDB1 in a synchronously rotating reference frame (u, v); (c) rotor motion radius and phase angle β of synchronous AMB force applied at the same time; (d) experimental results.

4.2 SMC control

Since the feedback signal reflects the phase change caused by the contact, reinforcing synchronous motion feedback signals in the control loop may be another

feasible re-levitation control method. Hence, a synchronous signal estimation based synchronous motion compensation (SMC) control was designed and applied to restore the rotor. The control diagram is shown in Fig. 15.

In SMC control, a synchronous signal estimator (blue part in Fig. 15) is activated to generate a synchronous motion signal if the contact event (red part in Fig. 15) occurs. The contact detection method is the same as PSSC. The output of the estimator is added to the feedback signal and the current saturation is considered.

The synchronous signal estimator can be a peak filter that is designed based on the Butterworth or other method. However, there is a trade-off between order and calculation speed. Too high an order will consume many resources and affect the control bandwidth. In addition, the synchronous signal estimator block in [24] can estimate the synchronous signal using limited calculations. Hence, it is applied in the following simulation. The magnitude and phase response of the synchronous signal estimator are shown in Fig. 16. The central frequency is the rotational frequency and there is almost no phase lag at the central frequency.

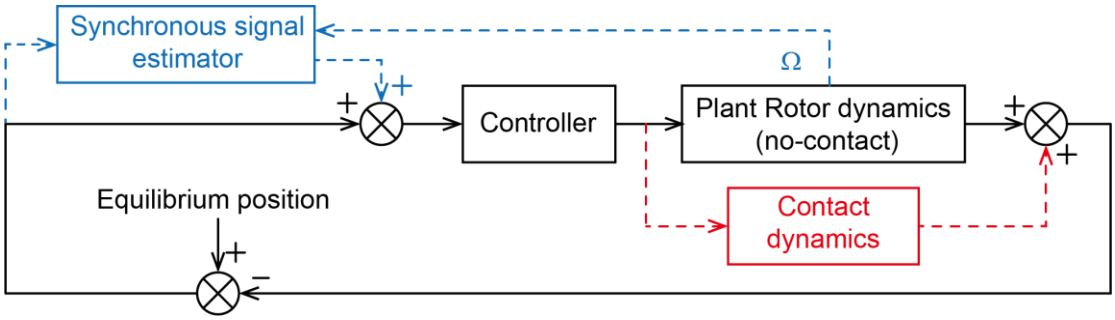

Figure 15. Synchronous motion compensation (SMC) control diagram

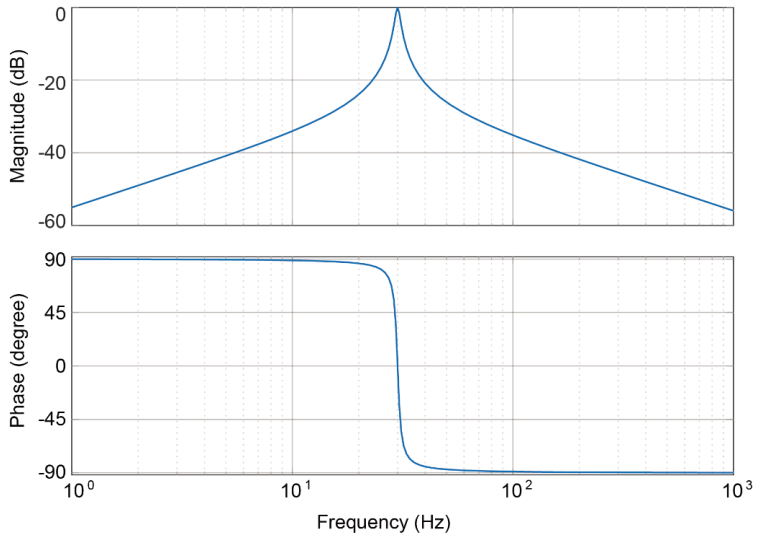

Figure 16. Magnitude-frequency and phase-frequency diagrams of the synchronous signal estimator

To compare the effects of the re-levitation control algorithms of SMC and PSSC, the control flow of the SMC control was set to be the same as that of the PSSC and

r_1, r_2 were also set as same value. Then, the AMB-rotor system with the SMC controller was simulated for the same shock contact event as in Fig. 14. Like Fig. 14, Figs. 17(a) and (b), respectively, show the simulation results of rotor trajectories at TDB1 in a fixed reference frame (*x, y*) and in a synchronously rotating reference frame (*u, v*), when SMC control was applied for shock contact. The SMC control restored the rotor orbit from the green triangle to the red dot. The motion radius of the rotor (as plotted in Fig. 17(c)) shows that SMC control was activated after approximately 0.1 s of contact. Then, the rotor radius dropped down, meaning the contact was destabilised successfully. The SMC control continued to run for Δt after the rotor radius dropped below r_2 (300 μm). The rotor recovered to normal operation within 1 s after contact, verifying the effectiveness of the SMC control on re-levitation.

To understand the shock contact and re-levitation processes more fully, the feedback signal, original feedback signal, and compensation signal with SMC control are shown in Fig. 17(d). The AMB forces of AMB2 in the x-axis with/without SMC are plotted in Fig. 17(e). Compared with Fig. 17(c), it is interesting to note that the AMB only produced a large electromagnetic force at the same time as the shock load. Instead of increasing to restore the rotor in the contact process induced by the shock load, the AMB force may even reduce with a traditional PID controller. This reduction of the AMB force is caused by the decrease of the rotor motion radius at AMB position shown in Fig. 17(f). It can be inferred that the position difference between the AMB and the TDB results in a reduction of rotor motion radius at the AMB position in the contact process.

In the limited time of SMC control, a small increase of AMB forces (caused by small synchronous motion signal compensation) can restore the rotor successfully, which means that the SMC re-levitation control has low energy consumption.

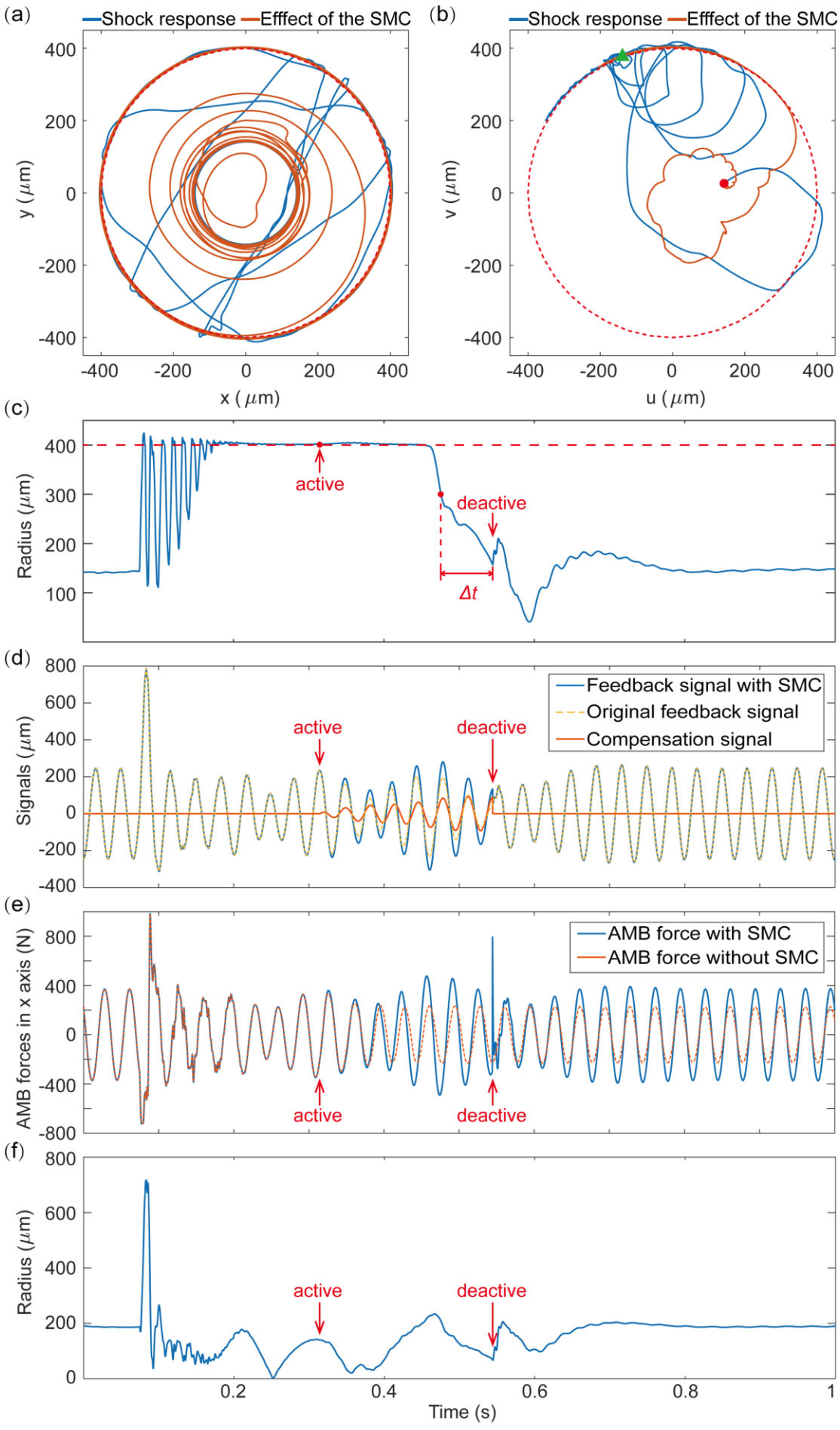
(a)
Shock response
Efffect of the SMC
y (μm)
x (μm)
(b)
Shock response
Efffect of the SMC
v (μm)
u (μm)
(c)
Radius (μm)
active
deactive
Δt
(d)
Signals (μm)
Feedback signal with SMC
Original feedback signal
Compensation signal
active
deactive
(e)
AMB forces in x axis (N)
AMB force with SMC
AMB force without SMC
active
deactive
(f)
Radius (μm)
active
deactive
Time (s)

Figure 17. Simulation results of SMC control. (a) rotor trajectories at TDB1 in a fixed reference frame (*x, y*); (b) rotor trajectories at TDB1 in a synchronously rotating reference frame (*u, v*); (c) motion radius of rotor at TDB1; (d) feedback signal, original feedback signal, and compensation signal of the SMC control; (e) AMB forces of AMB2 in the x-axis with/without SMC; (f) motion radius of rotor at AMB2.

4.3 Comparison

Comparing PSSC and SMC control, they are both open-loop compensation methods that do not affect the original stability of the control system. They both have clear and easy to understand control principles, can be applied online, and can recover the rotor to non-contact status automatically. However, there are some differences between the two methods, as presented in Table 1.

Table 1. Comparisons of PSSC and SMC control

Items	PSSC control	SMC control
Rotor recovery time	Uncertain, depends on difference between initial and required phases	Out of contact: within 0.2 s Recovery: within 1 s
Requirement of calculation speed	Low	Medium or High, may need higher calculation speed of hardware system
Safety	May further increase the contact force and damage the TDB and rotor	High

5. Conclusions

Bi-stable responses without/with contact behaviour and possible contact faults caused by shock loads in a rotor/AMB/TDB system have been investigated. Through theoretical analysis, it can be determined that rotational frequency, unbalance mass, friction coefficient, and control parameters are factors that determine the existence of bi-stable responses. These were observed through speed-up and -down experiments on an AMB-flexible rotor facility. Simulation and experimental results demonstrate that shock load is one of the potential trigger conditions that causes persistent contact. To destabilise persistent contact and restore contact-free levitation, PSSC control that uses an open-loop synchronous compensation force to destroy the force equilibrium was designed. The phase of the compensation signal increases ramp-like until rotor recovery. The effectiveness of PSSC is verified by simulation and experimental results. Then, SMC control, which aims to reinforce synchronous motion feedback signals, is also applied and re-levitates the rotor successfully. Finally, detailed similarities and differences between the two control methods are compared.

Future work will focus on the study of the contact dynamics and control of AMB systems with ball bearings as TDBs. New re-levitation control may need to be designed to deal with multimode shock responses such as bouncing contact and backward pure rolling.

References

[1] P. S. Keogh, C. Lusty, and N. Y. Bailey, “Nonlinear Dynamics and Control of Rotors Operating Within the Clearance Gaps of Magnetic Bearing Systems,” in Proceedings of the ASME 2017 International Mechanical Engineering Congress and Exposition, 2017, p. V04BT05A012.

[2] P. S. Keogh and M. O. T. Cole, “Rotor vibration with auxiliary bearing contact in magnetic bearing systems Part 1 Synchronous dynamics,” *Proc. Inst. Mech. Eng. Part C J. Mech. Eng. Sci.*, vol. 217, no. 4, pp. 377–392, 2003.

[3] P. S. Keogh, M. O. T. Cole, M. N. Sahinkaya, and C. R. Burrows, “On the Control of Synchronous Vibration in Rotor/Magnetic Bearing Systems Involving Auxiliary Bearing Contact,” *J. Eng. Gas Turbines Power*, vol. 126, no. 2, p. 366, 2004.

[4] M. Lyu, T. Liu, Z. Wang, S. Yan, X. Jia, and Y. Wang, “A control method of the rotor re-levitation for different orbit responses during touchdowns in active magnetic bearings,” *Mech. Syst. Signal Process.*, vol. 105, pp. 241–260, 2018.

[5] L. Hawkins, A. Filatov, S. Imani, and D. Prosser, “Test results and analytical predictions for rotor drop testing of an active megnetic bearing expander/generator,” *J. Eng. Gas Turbines Power*, vol. 129, no. 2, pp. 522–529, 2007.

[6] O. Halminen, A. Kärkkäinen, J. Sopanen, and A. Mikkola, “Active magnetic bearing-supported rotor with misaligned cageless backup bearings : A dropdown event simulation model,” *Mech. Syst. Signal Process.*, vol. 50–51, pp. 692–705, 2015.

[7] A. Kärkkäinen, J. Sopanen, and A. Mikkola, “Dynamic simulation of a flexible rotor during drop on retainer bearings,” *J. Sound Vib.*, vol. 306, no. 3–5, pp. 601–617, 2007.

[8] P. S. Keogh and M. O. T. Cole, “Contact Dynamic Response With Misalignment in a Flexible Rotor/Magnetic Bearing System,” *J. Eng. Gas Turbines Power*, vol. 128, no. 2, p. 362, 2006.

[9] P. S. Keogh, “Contact dynamic phenomena in rotating machines : Active / passive considerations,” *Mech. Syst. Signal Process.*, vol. 29, pp. 19–33, 2012.

[10] M. Schlotter and P. S. Keogh, “Synchronous Position Recovery Control for Flexible Rotors in Contact with Auxiliary Bearings,” *J. Vib. Acoust.*, vol. 129, no. 5, p. 550, 2007.

[11] M. Wang, M. O. T. Cole, and P. S. Keogh, “New LMI based gain-scheduling control for recovering contact-free operation of a magnetically levitated rotor,” *Mech. Syst. Signal Process.*, vol. 96, pp. 104–124, 2017.

[12] M. O. T. Cole and P. S. Keogh, “Rotor vibration with auxiliary bearing contact in magnetic bearing systems Part 2: Robust synchronous control for rotor position recovery,” *Proc. Inst. Mech. Eng. Part C J. Mech. Eng. Sci.*, vol. 217, no. 4, pp. 393–409, 2003.

[13] P. S. Keogh, M. N. Sahinkaya, and C. R. Burrows, “Wavelet Based Adaptation of H-infinity Control in Flexible Rotor / Magnetic Bearing Systems,” in *7th*

IFToMM-Conference on Rotor Dynamics, 2006, no. September, pp. 25–28.

[14] L. Ginzinger and H. Ulbrich, "Control of a rubbing rotor using an active auxiliary bearing," *J. Mech. Sci. Technol.*, vol. 21, no. 6, pp. 851–854, 2007.

[15] I. S. Cade, M. N. Sahinkaya, C. R. Burrows, and P. S. Keogh, "An Active Auxiliary Bearing Control Strategy to Reduce the Onset of Asynchronous Periodic Contact Modes in Rotor/Magnetic Bearing Systems," *J. Eng. Gas Turbines Power*, vol. 132, no. 5, p. 052502, 2010.

[16] P. Li, N. Sahinkaya, and P. Keogh, "Active Touchdown Bearing Control for Recovery of Contact-Free Rotor Levitation in AMB Systems," pp. 115–120, 2014.

[17] C. Jarroux, J. Mahfoud, B. Defoy, and T. Alban, "Stability of Rotating Machinery Supported on Active Magnetic Bearings Subjected to Base Excitation," *J. Vib. Acoust.*, vol. 142, no. 3, pp. 1–7, 2020.

[18] C. Jarroux, J. Mahfoud, R. Dufour, F. Legrand, B. Defoy, and T. Alban, "Dynamic Behavior of a Rotor-AMB System Due to Strong Base Motions," in *Proceedings of the 10th International Conference on Rotor Dynamics – IFToMM*, 2018, pp. 340–349.

[19] L. Hawkins, Z. Wang, and K. Nambiar, "Floating Shock Platform Testing of a Magnetic Bearing Supported Chiller Compressor – Measurements and Simulation Results," in *Proceedings of ASME Turbo Expo 2018 Turbomachinery Technical Conference and Exposition*, 2018, pp. 1–10.

[20] Y. Su, Y. Gu, P. S. Keogh, S. Yu, and G. Ren, "Nonlinear dynamic simulation and parametric analysis of a rotor-AMB-TDB system experiencing strong base shock excitations," *Mech. Mach. Theory*, vol. 155, p. 104071, 2021.

[21] P. S. Keogh and M. O.T. Cole, "Dynamic conditions to destabilize persistent Rotor/touchdown bearing contact in AMB systems," *Mech. Eng. J.*, vol. 4, no. 5, pp. 17-00005-17–00005, 2017.

[22] R. K. Khatri, L. A. Hawkins, and C. Bazergui, "Demonstrated operability and reliability improvements for a prototype high-speed rotary-disc atomizer supported on active magnetic bearings," in *Proceedings of ASME Turbo Expo 2015: Turbine Technical Conference and Exposition*, 2015, pp. 1–10.

[23] J. M. Nelson, H.D. and McVaugh, "The Dynamics of Rotor- Bearing Systems Using Finite Elements," *ASME J. Eng. Ind.*, vol. 98, pp. 593–600, 1976.

[24] R. Herzog, P. Bühler, C. Gähler, and R. Larsonneur, "Unbalance compensation using generalized notch filters in the multivariable feedback of magnetic bearings," *IEEE Trans. Control Syst. Technol.*, vol. 4, no. 5, pp. 580–586, 1996.